From phase space representation to amplitude equations in a pattern-forming experiment

To cite this article: C Gollwitzer *et al* 2010 *New J. Phys.* **12** 093037

View the article online for updates and enhancements.

New Journal of Physics

From phase space representation to amplitude equations in a pattern-forming experiment

C Gollwitzer[1], I Rehberg and R Richter[1]

Experimentalphysik V, Universität Bayreuth, D-95440 Bayreuth, Germany
E-mail: Christian.Gollwitzer@uni-bayreuth.de and
Reinhard.Richter@uni-bayreuth.de

Abstract. We describe and demonstrate a method to reconstruct an amplitude equation from the nonlinear relaxation dynamics in the neighbourhood of the Rosensweig instability. A flat layer of a ferrofluid is cooled such that the liquid has a relatively high viscosity. Consequently, the dynamics of the formation of the Rosensweig pattern becomes very slow. By a sudden switching of the magnetic induction, the system is pushed to an arbitrary point in the phase space spanned by the pattern amplitude and magnetic induction. Afterwards, it is allowed to relax to its equilibrium point. From the dynamics of this relaxation, we reconstruct the underlying fully nonlinear equation of motion of the pattern amplitude. The measured nonlinear dynamics helps us to select the best weakly nonlinear expansion that describes this hysteretic transition.

S Online supplementary data available from stacks.iop.org/NJP/12/093037/mmedia

---

[1] Authors to whom any correspondence should be addressed.

IOP Institute of Physics ⬥ DEUTSCHE PHYSIKALISCHE GESELLSCHAFT

Contents

1. Introduction

When Aristotle (350 B.C.) described the motion of falling bodies, he incorrectly claimed that the velocity is constant and is proportional to the mass of the body, because he did not know the concept of inertia. He was later proven wrong by Galilei (1638) and Newton (1687), who linked acceleration with forces. Aristotle's idea of motion, however, is a valid approximation in many cases, when a viscous fluid is involved and either the typical dimension d and the velocity v are small or the kinematic viscosity ν is high. In this limiting case of small Reynolds numbers $Re = vd/\nu \ll 1$, the viscous forces outweigh inertia, and the body and fluid motion is determined entirely by drag forces. Therefore, from a measurement of the velocity field, one immediately obtains the acting forces.

A similar dynamics is expected in the neighbourhood of a hydrodynamic instability, namely an amplitude equation of the form $\partial A / \partial t = f(A)$. The coefficients of these functions f can be determined experimentally. As an early example, Wesfreid *et al* (1978) accomplished this in a Rayleigh–Bénard convection experiment by observing the relaxation of the pattern amplitude following a jump in the control parameter. In this way, the coefficients of the amplitude equation of a pitchfork forward bifurcation to stripe-like patterns had been obtained. Here, we present such a measurement technique for a transcritical bifurcation to hexagons, which is characteristic for systems with broken up–down symmetry, i.e. a different universality class. As a specific example, we study the hexagonal arrangement of spikes forming in a layer of magnetic fluid.

Magnetic fluids, also known as ferrofluids, are colloidal suspensions of magnetic nanoparticles (Rosensweig 1985). When a vertically oriented magnetic field is applied to a horizontal layer of ferrofluid, a regular pattern of liquid spikes can appear above a certain threshold value of the magnetic induction B_c. This normal field instability was first reported by Cowley and Rosensweig (1967) and is, thus, also known as the Rosensweig instability. For an infinitely deep container, these authors provide also a linear stability analysis to find the critical threshold B_c of the magnetic induction and the critical wave number k_c. Their analysis works by computing the dynamics of a regular pattern in the vicinity of the threshold induction

and for very small amplitudes. This approach was later extended to calculate the viscosity-dependent growth rate by Salin (1993), and a finite depth of the container was taken into account by Weilepp and Brand (1996). For the case of a viscous magnetic fluid and an arbitrary layer thickness, Lange *et al* (2000) derived the growth rate and the wave number of maximal growth. The latter was experimentally determined and compared with the theoretical predictions in the same article and, later on, was compared with the wave number of the nonlinear state (Lange *et al* 2001). Lange (2001) calculated the growth rate for ferrofluids of different viscosities and eventually extended his analysis to the case of a nonlinear magnetization curve (Knieling *et al* 2007).

The nonlinear aspects of the dynamics have posed additional difficulties to the theoretical analysis (Lange 2002). Only recently, Bohlius *et al* (2007, 2008) successfully tackled the issue of systematically deriving nonlinear amplitude equations. For the amplitude A of hexagonal patterns these authors obtained

$$\tau_0 \frac{\partial A}{\partial t} = \varepsilon A + \gamma_1 A^2 - g A^3. \tag{1}$$

Here, τ_0 denotes a time scale, $\varepsilon = (B^2 - B_c^2)/B_c^2$ measures the distance from the bifurcation point, and γ_1 and g are expansion coefficients. The static solution of this amplitude equation coincides in structure with the result presented by Gailitis (1977) and by Kuznetsov and Spektor (1976), which was derived for magnetic susceptibilities $\chi \ll 1$ using an energy minimization approach. Using a similar approach, Friedrichs and Engel (2001) present a solution that is applicable up to $\chi \leqslant 0.4$. This solution is slightly different and corresponds to the amplitude equation with

$$\tau_0 \frac{\partial A}{\partial t} = \varepsilon A + \gamma_1 (1 + \varepsilon) A^2 - g A^3. \tag{2}$$

The difference from the cubic equation (1) is the additional factor $(1 + \varepsilon)$ in the quadratic term. The physical reasoning behind this higher-order correction is the scaling of the quadratic coefficient with B^2, which is proportional to $1 + \varepsilon = B^2/B_c^2$. In the limit of $\varepsilon \to 0$, both equations coincide. Now the question arises: Which of these solutions compares best to the experiment?

So far, the static solution of equation (2) was successfully fitted to the measured pattern amplitude for a ferrofluid with high susceptibility (Richter and Barashenkov 2005) and moderate susceptibility (Gollwitzer *et al* 2007). However, the amplitude equation (1) provides much more information, specifically on the nonlinear dynamics of the pattern formation. This has not yet been exploited. Knieling *et al* (2007) observed the nonlinear dynamics in a previous experiment and in related numerical simulations, but a quantitative comparison to an analytical model is performed only in the linear regime of the pattern growth.

The key idea in this paper is to use a fluid with a very high viscosity to study the pattern formation of the Rosensweig instability. Consequently, the Reynolds number is very small, $Re \approx 10^{-3}$, and the relaxation is monotonic and slow. The heavily overdamped system makes it easy to study the nonlinear dynamics quantitatively: due to the strong damping, the pattern amplitude follows a first-order equation of motion

$$\frac{\partial A}{\partial t} = f(\varepsilon, A) \tag{3}$$
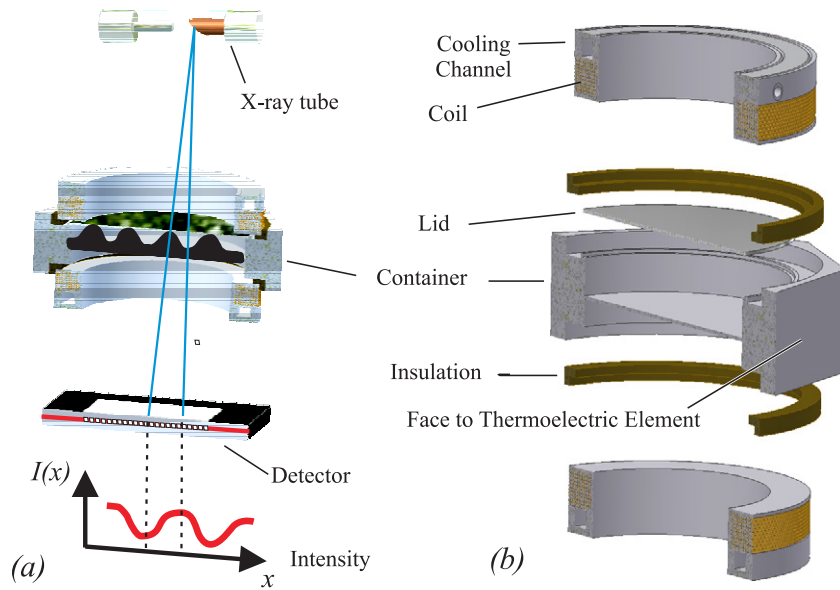
Figure 1. The apparatus for dynamic measurements of the Rosensweig instability. (a) Scheme of the assembled setup and (b) exploded view of the container with the coils.

even in the nonlinear regime. Here f is an analytic function that does not directly depend on time t. From the experimental data, f can be reconstructed and directly compared to the theoretical amplitude equations.

In the next section, we describe the experimental setup and the magnetic fluid we used. Subsequently, the measurement protocol and the data analysis are described. Then, the experimental data are compared to theoretical models, and finally the results are discussed.

2. Experimental setup

The experimental setup for the measurement of the surface deflections consists of an x-ray apparatus described in detail by Richter and Bläsing (2001). An x-ray point source emits radiation vertically from above through the container with a ferrofluid, which is placed midway between a Helmholtz pair of coils. Underneath the container, an x-ray camera records the radiation passing through the layer of ferrofluid. The intensity at each pixel of the detector is directly related to the height of the fluid above that pixel. Therefore, the full surface topography can be reconstructed after calibration (Gollwitzer *et al* 2007).

The container, which holds the ferrofluid sample, is depicted in figure 1(b). It is a regular octagon machined from aluminium with a side length of 77 mm and two concentric inner bores with a diameter of 140 mm. These circular holes are carved from above and below, leaving only a thin base in the middle of the vessel with a thickness of 2 mm. On top of the octagon, a circular lid is placed, which closes the hole from above (see figure 1(b)). Each side of the octagon is equipped with a thermoelectric element QC-127-1.4-8.5MS from Quick-Ohm. These are powered by a 1.2 kW Kepco KLP-20-120 power supply. The hot side of the thermoelectric elements is connected to water-cooled heat exchangers. The temperature is measured at the

Table 1. Material properties of the ferrofluid mark APG E32 (Lot G090707A) from Ferrotec Co.

Quantity		Value	Error	Unit
Density	ρ	1168	± 1	kg m^{-3}
Surface tension	σ	30.9	± 5	mN m^{-1}
Viscosity at $10\,^\circ\text{C}$	η	4.48	± 0.1	Pa s
Saturation magnetization	M_S	26.6	± 0.8	kA m^{-1}
Initial susceptibility at $10\,^\circ\text{C}$	χ_0	3.74	± 0.005	
Fit of $M(H)$ with the model by Ivanov and Kuznetsova (2001):				
Exponent of the Γ-distribution	α	3.8	± 1	
Typical diameter	d_0	1.7	± 0.2	nm
Volume fraction	ϕ	5.96	± 0.2	%
Critical induction from $M(H)$	B_c	10.5	± 0.1	mT

bottom of the aluminium container with a Pt100 resistor. A closed loop control, realized using a computer and programmable interface devices, holds the temperature θ of the vessel constant with an accuracy of 10 mK.

The container is surrounded by a Helmholtz pair of coils, thermally isolated from the vessel with a ring made from a flame-resistant composite material (FR-2). The size of the coils is adapted to the size of the vessel in order to introduce a magnetic ramp. With these coils, the magnetic field strength falls off towards the border of the vessel, where it reaches 80% of its value in the centre. The ramp is introduced in order to minimize the differences between the amplitudes obtained in a finite and an infinite geometry. For details of the magnetic ramp see Knieling *et al* (2010). Filling the container with ferrofluid enhances the magnetic induction in comparison with the empty coils for the same current I. Therefore, $B(I)$ is measured immediately beneath the bottom of the container, at the central position, and serves as the control parameter in the following.

We use the commercial ferrofluid APG E32 from Ferrotec Co., the basic material parameters of which are listed in table 1. The density was measured using a DMA 4100 density meter from Anton Paar. More problematic is the measurement of the surface tension. We measure the surface tension using a commercial ring tensiometer (LAUDA TE 1) and a pendant drop method (Dataphysics OCA 20). Both methods result in a surface tension of $\sigma = 31 \pm 0.5\,\text{mN m}^{-1}$, but when the liquid is allowed to rest for 1 day, σ drops down to $25 \pm 0.5\,\text{mN m}^{-1}$. This effect, which is not observed in similar but less viscous magnetic liquids like APG 512 a that was used in a previous work (Gollwitzer *et al* 2009), gives a hint that our liquid is chemically less stable in the sense that the surfactants change the surface tension on a longer time scale when the surface is changed. Since the pattern formation experiments do change the surface during measurements, the uncertainty of the surface tension is about $5\,\text{mN m}^{-1}$, as given in table 1.

The viscosity η deserves special attention for the experiments in this paper, as it influences the time scale of pattern formation. It has been measured in a temperature range of $-5\,^\circ\text{C} \leqslant \theta \leqslant 20\,^\circ\text{C}$ using a commercial rheometer (MCR 301, Anton Paar) in cone and plate geometry (figure 2). At room temperature, the ferrofluid we used has a viscosity $\eta = 2\,\text{Pa s}$, i.e. 2000 times
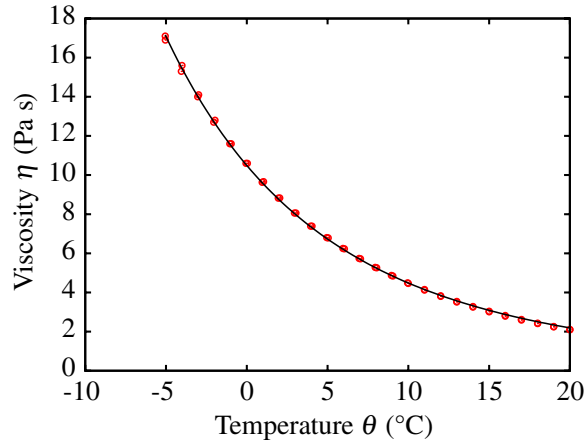
Figure 2. The dynamic viscosity η of the ferrofluid APG E32 versus the temperature θ. The symbols represent measurements, and the solid line is an approximation to equation (4).

the viscosity of water. This value can be increased by a factor of 9 when the liquid is cooled to $-5\,^\circ$C. The data from figure 2 can very well be fitted with the Vogel–Fulcher law (Rault 2000)

$$\eta = \eta_0 \, \exp\left(\frac{\psi}{\theta - \theta_0}\right), \tag{4}$$

with $\eta_0 = 0.48$ mPa s, $\psi = 1074$ K and $\theta_0 = -107.5\,^\circ$C, as indicated by the solid line in figure 2. This means that the viscosity can easily be adjusted in a wide range by controlling the temperature. For the present measurements, we chose a temperature of $\theta = 10\,^\circ$C, where the viscosity amounts to $\eta = 4.48$ Pa s according to equation (4).

The magnetization curve has been determined using a fluxmetric magnetometer consisting of a Helmholtz pair of sensing coils with 6800 windings and a commercial integrator (Lakeshore Fluxmeter 480). The sample is held in a spherical cavity with a diameter of 12.4 mm in order to provide a homogeneous magnetic field inside the sample with a demagnetization factor of $\frac{1}{3}$. The magnetization curve has been measured at a temperature of $\theta = 20\,^\circ$C (see figure 3). For a comparison with the pattern formation experiments, this curve must be extrapolated to $\theta = 10\,^\circ$C, which is done using the model by Ivanov and Kuznetsova (2001). Following Rosensweig (1985), section 7.1, from this curve and the material parameters a critical induction of 10.5 mT was estimated (cf table 1).

3. Measurement protocol

Figure 4 displays the measurement protocol on the basis of the bifurcation diagram. The static pattern amplitude of the Rosensweig instability in our fluid is indicated by the red line. When the system is set onto an arbitrary initial point $(B_{\text{ini}}, A_{\text{ini}})$ in this diagram and the magnetic induction B is kept constant, the amplitude A monotonically increases or decreases, until the system reaches stable equilibrium (solid red line). The direction of the change of A depends on the region where $(B_{\text{ini}}, A_{\text{ini}})$ is situated—in regions I and III in figure 4, A increases, and in regions II and IV, the amplitude decreases with time.
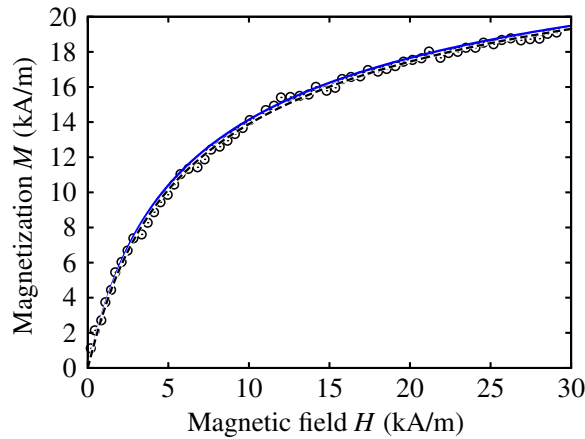
Figure 3. Magnetization curve of the ferrofluid APG E32. The symbols show the measured data at $\theta = 20\,^\circ$C. The black dashed line marks a fit with the model by Ivanov and Kuznetsova (2001). The blue solid line shows an extrapolation to $\theta = 10\,^\circ$C according to this model.
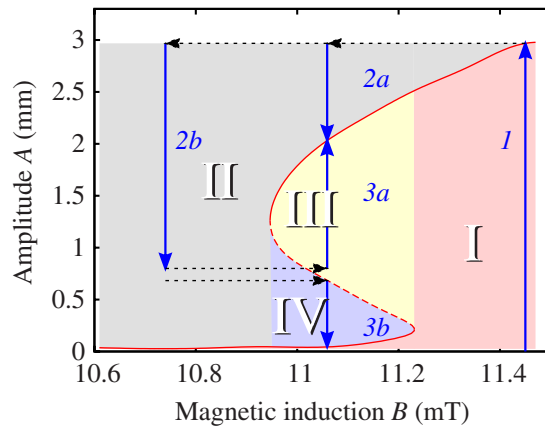

Figure 4. The multistep measurement protocol for the relaxation measurements. Dotted arrows indicate jumps of the magnetic inductions. Blue arrows denote the path of the system during the relaxation phases. A movie showing the sequence *1–2a* is available at stacks.iop.org/NJP/12/093037/mmedia.

In order to push the system to an arbitrary initial location $(B_{\text{ini}}, A_{\text{ini}})$, a multistep measurement protocol is employed. The first step (path *1*) is always a relaxation of the pattern in region I at the overcritical induction $B_{\text{high}} = 11.45$ mT for 1 min, to reach the final amplitude of $A_{\text{high}} = 2.98$ mm at that point. The corresponding pattern is shown in figure 5(a). To get to an arbitrary point in region II in figure 4, a second step is needed. When the system is settled at $(B_{\text{high}}, A_{\text{high}})$, the magnetic induction is quickly changed to the desired value B_{ini}, and the resulting dynamics is observed (path *2a*), until the final amplitude is reached. To get into the inner regions III or IV, three steps are needed in total—coming from $(B_{\text{high}}, A_{\text{high}})$, the second step (path *2b*) is a decay of the pattern amplitude at the subcritical induction $B_{\text{low}} = 10.74$ mT, until the intended initial amplitude A_{ini} is reached. The induction is then quickly raised to the desired B_{ini}. The system then follows the path *3a* or *3b* in region III or IV, respectively.
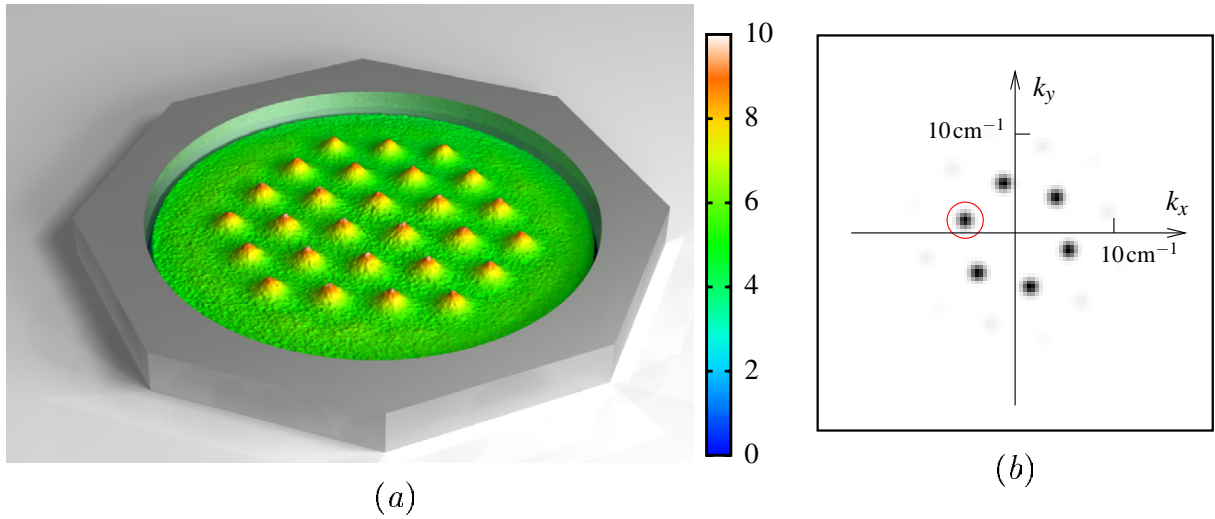
Figure 5. The final pattern at $B = 11.45$ mT. Panel (a) displays a reconstruction of the surface in real space. The outer dimension of the container is not to scale. The colour code gives the height of the liquid surface above ground in mm. The pattern amplitude is determined from the corresponding power spectrum shown in (b) by the total power in the encircled mode.

When the desired initial amplitude A_{ini} is zero, for example when the growth of the pattern in region I shall be observed, we also apply the three-step protocol with the detour by paths *1* and *2b*. At this point, the pattern decays until the amplitude is very small ($A_{ini} = 0.05$ mm). After that, the induction is raised to $B = B_{ini}$. We use this procedure instead of directly switching the magnetic induction from zero to $B = B_{ini}$ in order to establish the exactly same pattern in all regions. Coming from a perfectly flat surface, the pattern would have additional degrees of freedom manifesting themselves in point defects or different orientations of the wave vectors. When we take the detour by paths *1* and *2b*, we seed the wave vectors of the pattern at (B_{high}, A_{high}), and the final pattern developed is likely to be the same.

We explored all regions in figure 4 in several rounds. In the first round, we examined region I. We used the three-step procedure to observe the growth of the pattern from a very small amplitude up to the stable solution for 21 different inductions in the range 11.19 mT $\leqslant B \leqslant$ 11.46 mT. In the second round, we explored region II. Starting from $A_{ini} = A_{high}$ and 65 different inductions in the range 10.61 mT $\leqslant B \leqslant 11.46$ mT, the decay of the pattern was observed until it reaches the stable solution or zero. The third to sixth rounds covered regions III and IV. Starting from four different amplitudes, we observed the evolution of the pattern in the range of 10.89 mT $\leqslant B \leqslant 11.27$ mT. At each round, we recorded the complete evolution of the surface topography of the ferrofluid during the last step with the fastest possible frame rate (7.5 Hz) of the x-ray device, in total taking about 170 000 frames.

4. Data analysis

4.1. Reconstruction of the pattern amplitude

After processing the image data, we finally arrive at the surface topography for every frame. Figure 5(a) shows a reconstruction of the surface at $B = B_{high}$. A description of the technical

(a)   (b)
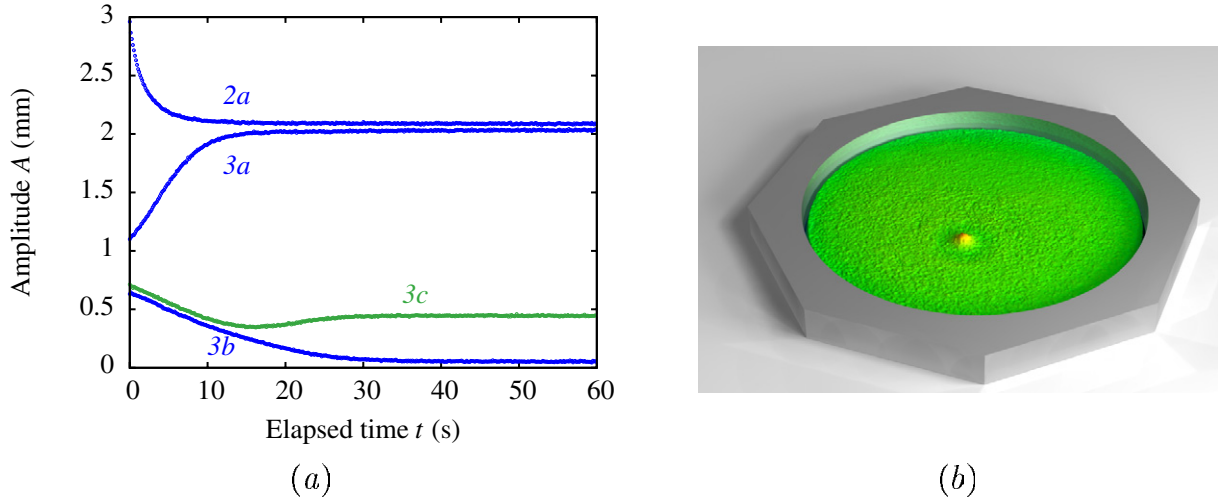
Figure 6. The evolution of the pattern amplitude at an induction $B = 11.06\,\text{mT}$, starting from different amplitudes (a). The labels of the datasets correspond to the paths in figure 4. Path *3c* ends in a localized state with only one spike (x-ray image shown in panel (b)), and has been removed at the data. A movie showing the temporal evolution of the pattern to the final state in panel (b) is available at stacks.iop.org/NJP/12/093037/mmedia.

details of this process can be found in the paper by Gollwitzer *et al* (2007). The amplitude of the pattern, *A*, is then determined in Fourier space (figure 5(b)). We use a circularly symmetric Hamming window with the weight function

$$
w(x, y) = \begin{cases} \left(0.54 + 0.46\cos\left(\dfrac{\pi\sqrt{x^2 + y^2}}{r_w}\right)\right)^2 & x^2 + y^2 \leqslant r_w^2 \\ 0 & \text{else} \end{cases} \tag{5}
$$

for apodization (Gollwitzer *et al* 2006) with a radius $r_w = 46\,\text{mm}$. The total power in one of the modes (marked with a red circle in figure 5(b)) is used to compute the amplitude of the pattern

$$
A = N \cdot \sqrt{\sum_j |c_j|^2}, \tag{6}
$$

where c_j are the Fourier coefficients inside the circle. In order to get a meaningful estimate, the normalization factor *N* is chosen such that *A* is the height difference between maxima and minima, when the input is a perfectly sinusoidal hexagonal pattern.

Figure 6(a) displays the resulting amplitude versus time for the paths labelled *2a*, *3a* and *3b* in figure 4. As expected from the bifurcation diagram, the amplitudes for paths *2a* and *3b* decrease monotonically, and the stable solution is approached in an asymptotic fashion. Similarly, *3a* increases monotonically and asymptotically converges to the patterned state. There is, however, a small glitch. The bifurcation figure 4 provides only a single solution for the patterned state, but the asymptotic amplitudes of paths *2a* and *3a* differ by 2.6%. The reason is that the final pattern is different in spite of the aforementioned efforts—path *2a* ends in a pattern with 20 spikes, whereas the final pattern of path *3a* contains only 11 spikes. These additional

spikes are situated near the border of the window function and therefore contribute only a little to the overall amplitude. A further path, *3c*, which starts very close to the initial amplitude of the path *3b*, ends in a finite intermediate amplitude. Path *3c* finally ends in a localized solution with only a single spike as depicted in figure 6(b).

The present setup does not allow us to control these additional degrees of freedom for the fluid surface experimentally. Because localized states are not described by the amplitude equations derived for spatially homogenous hexagonal patterns, we have to disregard patterns that are too different from that assumption for a meaningful comparison with those theories. Precisely speaking, those data sets have been sorted out where the final pattern did not fill the full-width at half-maximum of the window function, which is the case for less than ten spikes. This somewhat arbitrary number can partly be defended by the fact that the amplitude would be underestimated by more than 9% due to the window used in our data processing. Moreover, it is known that the amplitude of localized states differs from the one for homogeneous patterns (Richter and Barashenkov 2005), but a precise knowledge about the difference between these amplitudes is currently not available.

Out of 205 data sets, 32 have been rejected, the final pattern of which consists of only a small number of spikes. Every pattern from a single spike up to a cluster of 9 has been found, whereas the fully developed pattern contains up to 27 spikes. These patterns emerged in the bistable regime of the fully developed pattern and have been previously observed by Richter and Barashenkov (2005). In their experiment, the localized spikes have been initiated by a local disturbance of the magnetic induction. In the present experiment, these patterns emerge spontaneously from a starting point $(B_{\text{ini}}, A_{\text{ini}})$ near the unstable solution branch. In this study, however, we focus only on the fully developed patterns.

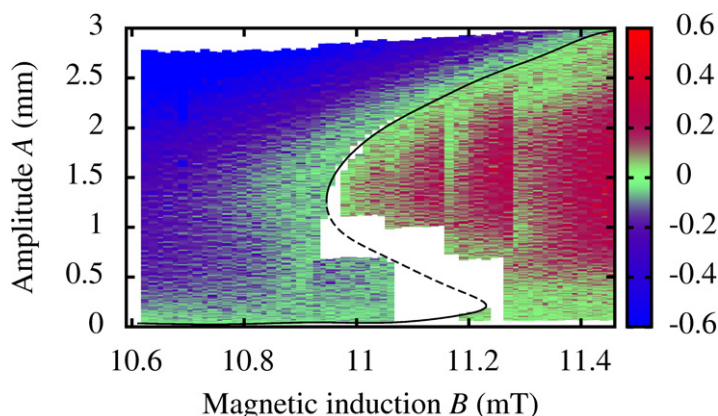### 4.2. Recovery of the amplitude equation

In the following, we will describe a method to extract the amplitude equation from the experimental data. So far, we have measured the evolution of the amplitude $A(t)$ for different values of the induction B and a set of initial amplitudes A_{ini}. Suppose that the system can indeed be described by an amplitude equation of the form (3). Then $A(t)$ is the solution of this equation for different initial conditions $(B_{\text{ini}}, A_{\text{ini}})$, and we want to get the function f on the right-hand side of (3). Because this function should not depend on time, the time derivative $\dot{A} = \partial A/\partial t$ of our measured $A(t)$ directly gives the value of this function at the corresponding amplitude. We therefore plot $\dot{A}$ as a function of A in figure 7 for one selected induction in the bistable region. The time derivative has been estimated from the measured data by central differences (Abramowitz and Stegun 1965, section 25.1.2)

$$
\begin{aligned}
\left.\frac{\partial A}{\partial t}\right|_{n+\frac{1}{2}} &\approx \frac{A_{n+1} - A_n}{\Delta t} \\
A|_{n+\frac{1}{2}} &\approx \frac{A_{n+1} + A_n}{2},
\end{aligned}
\tag{7}
$$

where $\Delta t = 0.134$ ms is the time between consecutive frames, and A_i denotes the pattern amplitude of the ith frame. The plot in figure 7 comprises three different data sets. The sets *2a* and *3a* stem from a relaxation to a pattern amplitude of about 2 mm; the set *3b* describes the decay to a flat surface layer. Because the time derivative of the experimental data suffers heavily from noise, we also plot a smooth approximation explained later in section 5 as a guide
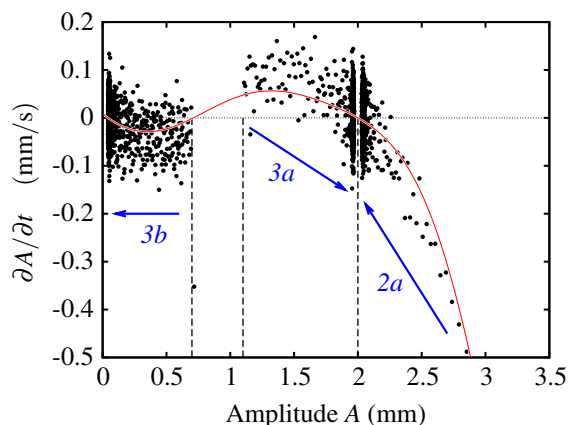
Figure 7. Reconstruction of the amplitude equation at an induction $B = 11.05$ mT. The symbols are central differences from equation (7). The red line serves as a guide to the eye and is obtained from the data by equation (8). The blue arrows indicate the range of the corresponding data sets presented in figure 6(a).

Figure 8. The measured amplitude dynamics for the whole phase space. The colour indicates the velocity $\partial A/\partial t$ in mm s^{-1}. Red (blue) means rising (falling) amplitude, respectively. Green indicates the zero (root of the amplitude equation).

to the eye (red line in figure 7). In the bistable regime, the amplitude equation has three roots, corresponding to one unstable and two stable solutions. In figure 7, these stable and unstable solutions are characterized by zero-crossings with a negative or positive slope, respectively.

5. Experimental results

Figure 8 displays the dynamics of the amplitude determined from equation (7) in the full range of A and B. The colour indicates the sign and strength of the 'force' $f(B, A)$ and confirms the bifurcation diagram suggested in figure 4. However, the data points are not only affected by noise, but also they are irregularly distributed. The density is high at the stable solution branch,

and on the contrary there are voids in the diagram, where data are not available at all. These voids belong to data sets that have been sorted out, because they converge to a localized solution (cf section 4.2).

In order to further interpret the data, a smooth approximation is helpful. The next section shows a way to construct such an approximation. Thereafter it is compared with analytical model equations (section 5.2)

5.1. Approximation with radial basis functions (RBFs)

We use a multiquadric RBF network to compute a smooth sensible approximation to the amplitude equation (Powell 1990). An RBF network is a linear combination of shifted basis functions

$$s(\boldsymbol{x}) = \sum_j \lambda_j \phi(\|\boldsymbol{x} - \boldsymbol{c}_j\|) + p(\boldsymbol{x}), \tag{8}$$

with the weights λ_j, a basis function ϕ, the arbitrarily chosen centres $\boldsymbol{c}_j$ and the low-order multivariate polynomial $p(\boldsymbol{x})$. We choose the multiquadric basis function

$$\phi(x) = \sqrt{1 + x^2} \tag{9}$$

and a linear polynomial $p(\boldsymbol{x})$. The vector $\boldsymbol{x}$ is a scaled combination of the coordinates of the phase space

$$\begin{aligned} \boldsymbol{x} &= (B/\delta_B, A/\delta_A), \\ \delta_B &= 0.2 \, \text{mT}, \\ \delta_A &= 1 \, \text{mm}. \end{aligned} \tag{10}$$

The scale variables $\delta_{A,B}$ are chosen according to the empirical rule that they should be approximately equal to the distance between centres in the corresponding direction.

RBF networks with the basis function (9) are infinitely differentiable and thus well suited to the approximation of smooth functions. This kind of approximation has been proven useful in many applications. For an overview, see the review by Hardy (1990).

Figure 9 displays the result from fitting the measured data from figure 8 with equation (8). The centres $\boldsymbol{c}_j$ can be chosen almost arbitrarily; we have selected 50 centres equally distributed in the measured region and additionally placed 68 centres near the stable solution branch. The location of these 118 centres is marked in figure 9 by the blue crosses.

Only the weights λ_j in equation (8) are adjusted, while the position of the centres $\boldsymbol{c}_j$ are held constant. The problem of adjusting equation (8) to our data is therefore reduced to a general linear least-squares fitting problem with 118 free parameters. In order to avoid the problem of overfitting, we do not fit the data directly with equation (8), but instead apply Tikhonov regularization (Neumaier 1998)

$$\sum_j |s(\boldsymbol{x}_j) - f(\boldsymbol{x}_j)|^2 + \xi \sum_k \lambda_k^2 = \text{min}!, \tag{11}$$

where $f(\boldsymbol{x}_j)$ are the measured data and ξ is the regularization parameter. This parameter controls the complexity of the model. A value near zero results in a standard least-squares fit of the model to the data, while a larger value makes the resulting model more smooth. To find the optimal value of the regularization parameter, we apply standard twofold cross validation (Picard and Cook 1984), which yields an optimal regularization parameter of $\xi = 0.4$.
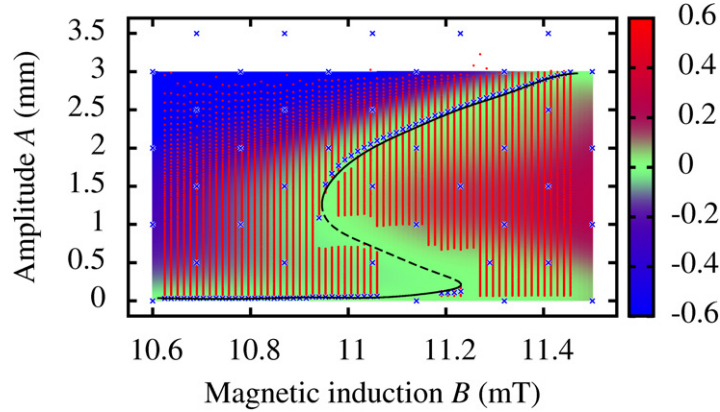
Figure 9. The multiquadric RBF approximation of $\partial A/\partial t\,(A, B)$. The colour indicates this velocity in $\mathrm{mm\,s^{-1}}$. The red dots correspond to the measured data. The blue crosses show the position of the centres of the radial basis functions. The black solid (dashed) line represents the stable (unstable) zero of the approximant.

The zero from this fit gives an estimate for the stable and unstable solutions of the amplitude equation and is indicated by the solid and dashed black lines in figure 9, respectively. For comparison, the original data are also shown with the red dots. The RBF reconstruction of the solution gives a very plausible result, which captures the essential features of the raw data, namely the imperfection, and provides an estimate for the unstable solution, which can only be approached to a certain limit by this method (see the voids in figure 8). This result of the RBF reconstruction has also been used to display the equilibrium in figures 4 and 8 above.

Such an approximation of the measured data by an RBF network has proven useful to get an unbiased estimate of the equilibrium and to fill in missing data. However, such a non-parametric regression technique cannot provide physically meaningful parameters (Green and Silverman 1994). In the next section, we compare the experimental data with nonlinear model equations for the bifurcation.

5.2. Comparison to nonlinear model equations

A model equation for the imperfect, hysteretic bifurcation diagram like in figure 4 is given by

$$\tau_0 \frac{\partial A}{\partial t} = \varepsilon A + \gamma_1 \left(1 + \gamma_2 \varepsilon\right) A^2 - g A^3 + b, \tag{12}$$

where τ_0 denotes a time scale and $\varepsilon = (B^2 - B_c^2)/B_c^2$ measures the distance from the bifurcation point (Reimann *et al* 2005). For the diagram depicted in figure 4, γ_1 must be positive, and the width of the hysteresis increases with the magnitude of γ_1. In order to get stable patterns for $\varepsilon > 0$, g must be positive, and the final amplitude decreases with the magnitude of g. The constant term b represents the imperfection of the system. For $b > 0$, the transcritical bifurcation at $\varepsilon = 0$, $A = 0$ dissolves into two saddle–node bifurcations, the distance of which is controlled by the magnitude of b.

In the perfect case ($b = 0$) and for $\gamma_2 = 0$, equation (12) simplifies to equation (1). For $\gamma_2 = 1$, equation (12) comprises the amplitude equation (2), where the quadratic term is augmented by the factor $(1 + \varepsilon)$. From a formal point of view, one might ask whether this

Table 2. The different models and their coefficients (columns 1–5). To elucidate their applicability to the experimental data we compare the width ΔB_{hyst} of the bistable regime, the integral deviation $\aleph$ of the static solutions from the RBF approximation in the investigated range $A \in [0.04\,\text{mm}\ldots 2.97\,\text{mm}]$, and the residual sum of squares $\hat{\chi}^2$ of all time-dependent data (columns 6–8). For the amplitude equations, also the critical threshold B_{c} is given in the last column.

Model	τ_0 (s)	γ_1 $(1\,\text{mm}^{-1})$	γ_2	g $(1\,\text{mm}^{-2})$	b (mm)	ΔB_{hyst} (mT)	$\aleph$ 10^{-6}	$\hat{\chi}^2$ $(\text{mm s}^{-1})^2$	B_{c} (mT)
Equation (1)	0.4897	0.0773	0	0.0297	0.0013	0.1809	7.58	327.638	11.27
Equation (2)	0.5933	0.1171	1	0.0407	0.0024	0.2468	2.56	326.834	11.40
Equation (12)	0.5770	0.1111	0.891	0.0391	0.0023	0.2372	2.85	326.816	11.39
RBF	N/A	N/A	N/A	N/A	N/A	0.2834	N/A	278.12	N/A

additional factor could also incorporate another adjustable parameter, the blend parameter γ_2, resulting in the more general equation (12). Therefore, a comparison of the experimental data with this equation provides some hint of whether it is empirically advantageous to incorporate the ε-dependence in the quadratic coefficient.

The coefficients in equations (1) and (2) are in principle given by Bohlius *et al* (2008) and Friedrichs and Engel (2001), respectively, as functions of the material parameters. However, these analyses are carried out for a linear magnetization curve $M(H) = \chi H$ and, in the latter case, small values of χ only, and therefore cannot be directly applied to our fluid. By treating τ_0, B_{c}, γ_1, γ_2, g and b as adjustable parameters, these equations can nevertheless be fitted to the measured data. The coefficients are listed in table 2.

Figure 10 displays the result of fitting the model equations to the experimental data together with the neutral curve of the RBF approximation (white line) for reference. At a first glance, all models give reasonable approximations to the experimental data and the differences are minor. One such difference becomes apparent when looking at the equilibrium line (black solid line). The experimental data (red dots) evidently contain the final static amplitude in almost all cases, so the equilibrium should pass through or very near the endpoints of the experimental data lines. This condition does not hold for the plain cubic equation in figure 10(a). The width of the bistable regime ΔB_{hyst} suggested by the experimental data amounts to 0.29 mT, but the cubic equation provides only 0.18 mT (cf table 2). Equation (2), which is augmented with $(1 + \varepsilon)$, gives a much better approximation of the equilibrium line (figure 10(b)). Here, the width of the hysteresis amounts to 0.25 mT, which is better but still smaller than the true value. Finally, equation (12), which is a blend of the two former models, scores in between them in this test with $\Delta B_{\text{hyst}} = 0.24$ mT (figure 10(c)). The comparison of ΔB_{hyst} takes only the two saddle-node points into account. To compare the whole equilibrium line, we provide an integral measure, namely the deviation in B on the static solution

$$\aleph = \frac{1}{A_{\text{max}} \cdot \bar{B}_{\text{c}}^2} \int_0^{A_{\text{max}}} (B_{\text{RBF}} - B)^2 \, \text{d}A, \tag{13}$$

which is integrated over the whole amplitude range covered in the experiment. Here, B_{RBF} serves as a smooth approximation to the experimental data, and $\bar{B}_{\text{c}} = 11.36$ mT is the mean value of the critical inductions of the three model equations.
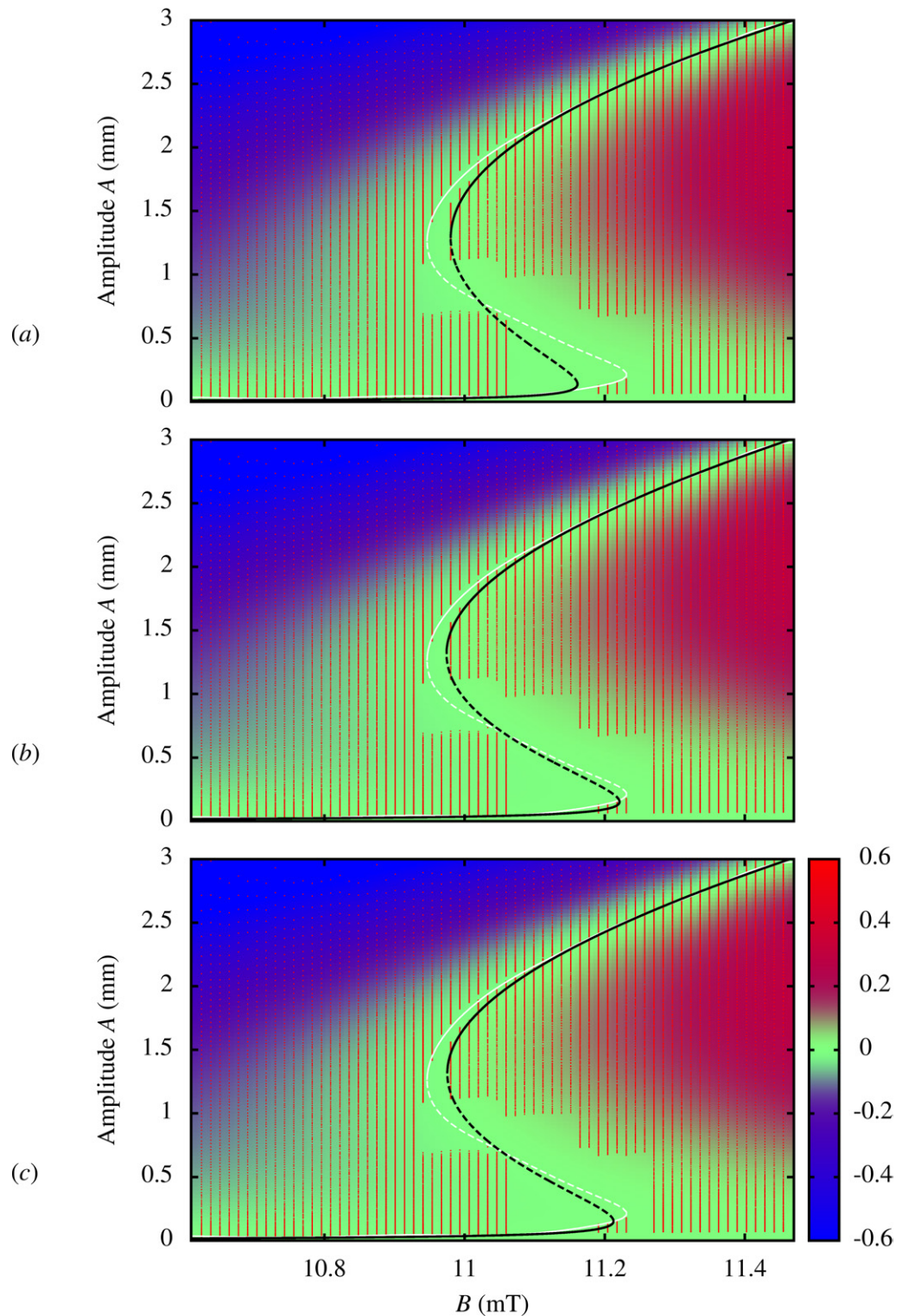
Figure 10. Comparison of different models for the amplitude equation. (a) Cubic equation (1), (b) augmented equation (2) and (c) blended equation (12) with $\gamma_2 = 0.755$. The white line is the neutral curve obtained from the RBF approximation, whereas the black line and the colour code come from the corresponding model.
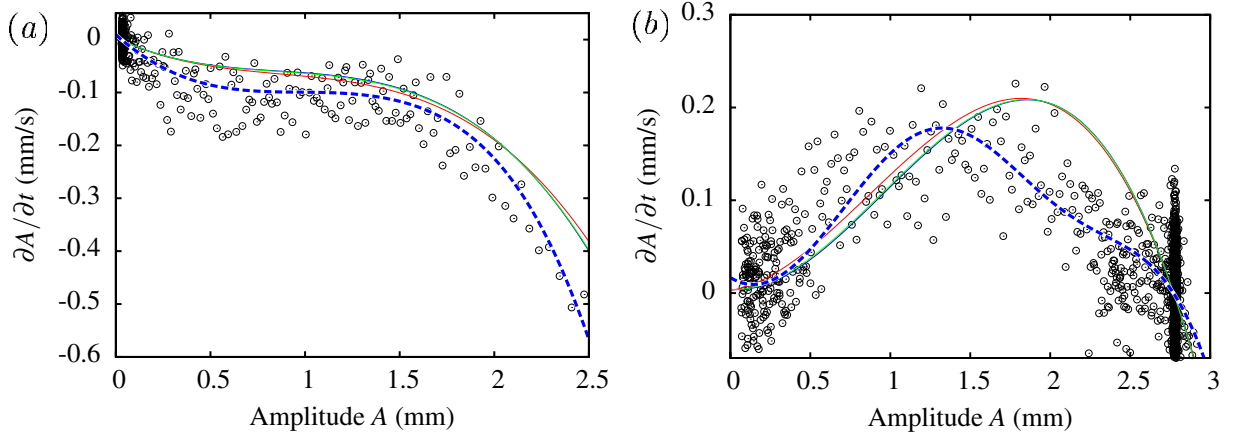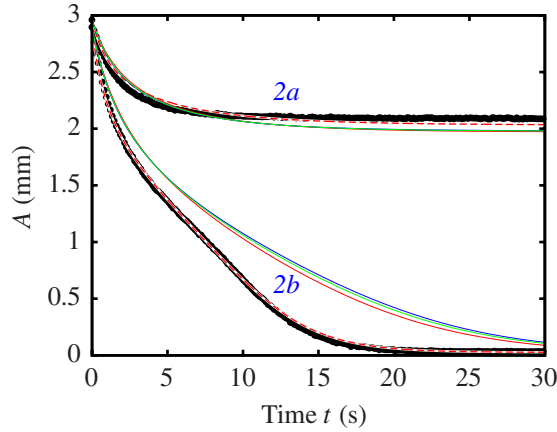
Figure 11. Comparison of the amplitude equations for a constant induction $B = 10.80 \, \text{mT}$ (a) and $B = 11.35 \, \text{mT}$ (b). The symbols display the original measured data, the dashed line is the RBF approximation and the solid lines represent the parametric model equations (1, red), (2, blue) and (12, green).

For a list of ℵ, see the 7th column of table 2. In this measure, the augmented equation (2) comes closer to the RBF by a factor of 3. Both inspected measures, ΔB_{hyst} and ℵ, demonstrate that the augmented equation (2) provides a better approximation than the pure cubic equation (1). A description by the blended model (12) yields a best fit blend parameter $\gamma_2 = 0.891$. This tends more to the augmented equation (2) than to the plain cubic equation (1). It is thus safe to conclude that equation (2) provides a wider range of applicability compared to equation (1), with the same number of adjustable parameters.

Even though the equilibrium curve can be represented reasonably well by at least the augmented amplitude equation, the fitted models all deviate from the measured data off the equilibrium curve in two ways. At small inductions, the model equations underestimate the velocity of the pattern decay. Figure 11(a) depicts the amplitude equations for an undercritical induction of $B = 10.80 \, \text{mT}$. Here, the model equations all yield approximately the same result, but the difference compared to the measured data is roughly 30%. At overcritical inductions (figure 11(b)), the model equations culminate around $A = 2 \, \text{mm}$, while the RBF approximation has its maximum around 1.5 mm, which coincides with the experimental observation.

The quality of the theoretical descriptions becomes apparent especially when comparing the temporal evolution of the amplitude with numerical solutions of the amplitude equations, as shown in figure 12. These solutions are obtained by solving for A in equations (1), (2), and (12), with the first experimental data point as the initial condition. The solutions in the bistable regime (path *2a*) describe the relaxation well, whereas path *2b*, observed at lower induction, differs notably from the integrated solution. This difference results from the underestimation of the decay rate far from the critical point, which was discussed above. Of course, the model equations are expansions about the critical point, and are not expected to be accurate far from the critical induction. In contrast, the temporal relaxation obtained from the RBF network fits the experimental data well for both paths.

Figure 12. Comparison of the time evolution of the amplitude for paths *2a* and *2b* with the integrated model equations. The black dots display the original measured data; the lines represent the solution of equation (3) for different right-hand sides, namely RBF (red dashed line) and the amplitude equations (1, red), (2, blue) and (12, green).

A quantitative measure for the deviations of the model equations $s(\boldsymbol{x}_j)$ from the experimental data $f(\boldsymbol{x}_j)$ is given by the sum of squared residuals

$$\hat{\chi}^2 = \sum_j \left| s(\boldsymbol{x}_j) - f(\boldsymbol{x}_j) \right|^2. \tag{14}$$

For the computation of $\hat{\chi}^2$, the dynamic evolution of the amplitudes in the whole range of the control parameter has been taken into account. The resulting values of $\hat{\chi}^2$ are listed in the 8th column of table 2. The values obtained for equations (1), (2) and (12) are larger than the one obtained for the RBF approximation. This indicates that the dynamics away from the equilibrium curve is better described by the latter approximation. Note that in contrast to $\aleph$, $\hat{\chi}^2$ cannot discriminate between the different model equations (1), (2) and (12).

For the overcritical induction, also the RBF approximation shows artefacts, as can be seen in figure 11(b). The measured data suggest a smooth shape of the amplitude equation, while the RBF approximation shows a bump near $A = 2, \ldots, 2.5$ mm. This irregularity stems from the double equilibrium point, which can be seen in figure 6 (cf traces *2a* and *3a*) and figure 7. These double equilibrium points represent similar but different stable patterns and exist also in the neighbourhood of the data shown in figure 11(b). They influence the RBF network, because it is a global approximation scheme.

6. Discussion and outlook

Using a highly viscous ferrofluid, the evolution of the pattern caused by the Rosensweig instability can be slowed down to the order of minutes. Therefore, it is possible to conveniently observe the dynamics using a two-dimensional imaging technique based on the absorption of x-rays. We have explored the full phase space in the vicinity of a hysteresis loop formed by a transcritical bifurcation and a saddle node. From the measured data we have reconstructed a nonlinear equation of motion. A smooth approximation of the noisy experimental data

with RBFs provides an estimate for missing data and for the static amplitude. Amplitude equations for the instability were successfully fitted to the experimental data. The estimate of the equilibrium curve based on the cubic amplitude equation, as derived by Bohlius *et al* (2008), can be significantly improved by augmenting the quadratic coefficient with the factor $(1+\varepsilon)$. This factor can be extracted from the free energy functional of Friedrichs and Engel (2001) and reduces the deviation $\aleph$ between the equilibrium curve and the RBF reference by a factor of three.

However, a comparison of the absolute magnitude of both amplitude equations with the experimental data at an induction 5% below the critical induction B_c reveals that neither amplitude equation can exactly describe all of the recorded dynamics. At least the agreement between the experiment and the model equations is within 30%. This is surprising considering the fact that these equations are low-order expansions about the critical threshold B_c, while the investigated range of about 7.5% of B_c even includes another critical point at a saddle node. Moreover, this 30% agreement is already quite useful for practical estimates considering the fact that the amplitude equations are convenient algebraic expressions containing only three parameters.

So far, the experimentally determined expansion coefficients cannot be sensibly compared with the ones derived by theory, because the latter does not include a nonlinear magnetization curve, which has a major influence on the instability. For example, for our fluid the critical threshold B_c is shifted by about 10% . The change in the expansion coefficients is unknown. Its calculation remains a challenge for theory.

While we have extracted a nonlinear equation of motion for the specific example of the Rosensweig instability, it is worth mentioning that the method is applicable to a wide set of overdamped pattern-forming systems. A necessary precondition is that the control parameter can be switched much faster than the characteristic relaxation time.

In this paper, only space-filling homogeneous patterns have been considered for the method. However, the real system has additional degrees of freedom, which are manifested in the formation of localized states as observed previously by Richter and Barashenkov (2005). Whereas in the latter work a local disturbance of the magnetic induction was needed to ignite localized states, here localized spikes and hexagonal patches emerge spontaneously when the measurement protocol pushes the system into the neighbourhood of the unstable branch.

While a nuisance for the particular task of this paper, this multistability of solitary spikes, hexagonal patches and the homogeneous hexagonal state is an interesting phenomenon in itself. It might be possible to describe all these patterns as a single solution containing multiple foldings, which is the basic idea of the homoclinic snaking scenario discussed in this connection (see e.g. Lloyd *et al* 2008). From an experimental point of view, building a specialized apparatus for controlling the transitions between these different patterns seems desirable for a detailed comparison, but it is yet to be designed.

Acknowledgments

IOP Institute of Physics ⬥ DEUTSCHE PHYSIKALISCHE GESELLSCHAFT

References

Abramowitz M and Stegun I 1965 *Handbook of Mathematical Functions: With Formulas, Graphs, and Mathematical Tables* 9th edn (New York: Courier Dover Publications)

Aristotle 350 B.C. *Physics* (Athens)

Bohlius S, Brand H R and Pleiner H 2008 *Prog. Theor. Phys. Suppl.* **175** 27

Bohlius S, Pleiner H and Brand H R 2007 *Phys. Fluids* **19** 094103

Cowley M D and Rosensweig R E 1967 *J. Fluid Mech.* **30** 671

Friedrichs R and Engel A 2001 *Phys. Rev.* E **64** 021406

Gailitis A 1977 *J. Fluid Mech.* **82** 401

Galilei G 1638 *Discorsi e dimostrazioni matematiche* (Leiden: Elsevier)

Gollwitzer C, Matthies G, Richter R, Rehberg I and Tobiska L 2007 *J. Fluid Mech.* **571** 455

Gollwitzer C, Rehberg I and Richter R 2006 *J. Phys.: Condens. Matter* **18** 2643

Gollwitzer C, Spyropoulos A N, Papathanasiou A G, Boudouvis A G and Richter R 2009 *New J. Phys.* **11** 053016

Green P and Silverman B 1994 *Nonparametric Regression and Generalized Linear Models: A Roughness Penalty Approach* (London: Chapman and Hall/CRC)

Hardy R 1990 *Comput. Math. Appl.* **19** 163

Ivanov A O and Kuznetsova O B 2001 *Phys. Rev.* E **64** 041405

Knieling H, Rehberg I and Richter R 2010 *Phys. Procedia* submitted

Knieling H, Richter R, Rehberg I, Matthies G and Lange A 2007 *Phys. Rev.* E **76** 66301

Kuznetsov E A and Spektor M D 1976 *Sov. Phys.—JETP* **44** 36

Lange A 2001 *Europhys. Lett.* **55** 327

Lange A 2002 *Int. J. Mod. Phys.* B **16** 1155

Lange A, Reimann B and Richter R 2000 *Phys. Rev.* E **61** 5528

Lange A, Reimann B and Richter R 2001 *Magnetohydrodynamics* **37** 261

Lloyd D, Sandstede B, Avitabile D and Champneys A 2008 *SIAM J. Appl. Dyn. Syst.* **7** 1049

Neumaier A 1998 *SIAM Rev.* **40** 636

Newton I 1687 *Philosophiae Naturalis Principia Mathematica* (London: Royal Society)

Picard R R and Cook R D 1984 *J. Am. Stat. Assoc.* **79** 575

Powell M J D 1990 *Advances in Numerical Analysis, Vol 2: Wavelets, Subdivision Algorithms and Radial Basis Functions* ed W Light (Oxford: Oxford University Press) p 105–210

Rault J 2000 *J. Non-Cryst. Solids* **271** 177

Reimann B, Richter R, Knieling H and Rehberg I 2005 *Phys. Rev.* E **71** 055202

Richter R and Barashenkov I 2005 *Phys. Rev. Lett.* **94** 184503

Richter R and Bläsing J 2001 *Rev. Sci. Instrum.* **72** 1729

Rosensweig R E 1985 *Ferrohydrodynamics* (Cambridge: Cambridge University Press)

Salin D 1993 *Europhys. Lett.* **21** 667

Weilepp J and Brand H R 1996 *J. Physique* II **6** 419

Wesfreid J, Pomeau Y, Dubois M, Normand C and Bergé P 1978 *J. Physique Lett.* **39** 725